Exciton Binding Energy and the Nature of Emissive States in Organometal Halide Perovskites

10 AUTHORS, INCLUDING:

Mohamed Abdellah
Lund University
29 PUBLICATIONS **375** CITATIONS

SEE PROFILE

Maria E Messing
Lund University
62 PUBLICATIONS **1,080** CITATIONS

SEE PROFILE

Sophie E. Canton
107 PUBLICATIONS **675** CITATIONS

SEE PROFILE

Tönu Pullerits
Lund University
180 PUBLICATIONS **5,471** CITATIONS

SEE PROFILE

Exciton Binding Energy and the Nature of Emissive States in Organometal Halide Perovskites

Kaibo Zheng,[†] Qiushi Zhu,[§] Mohamed Abdellah,[†,‡] Maria E. Messing,[∥] Wei Zhang,[†] Alexander Generalov,[⊥] Yuran Niu,[⊥] Lynn Ribaud,[#] Sophie E. Canton,*,[∇,○] and Tõnu Pullerits*,[†]

[†]Department of Chemical Physics, Lund University, Box 124, 22100, Lund, Sweden

[‡]Department of Chemistry, Qena Faculty of Science, South Valley University, Qena 83523, Egypt

[§]Department of Synchrotron Radiation Instrumentation, Lund University, Box 118, 22100, Lund, Sweden

[∥]Deptartment of Solid State Physics, Lund University, Box 118, 22100, Lund, Sweden

[⊥]MAX IV Laboratory, Lund University, Box 118, 22100, Lund, Sweden

[#]X-ray Science Division, Advanced Photon Source and Materials Science Division, Argonne National Laboratory, Argonne, Illinois 60439, United States

[∇]IFG Structural Dynamics of (Bio)chemical Systems, Max Planck Institute for Biophysical Chemistry, Am Fassberg 11, D-37077 Goettingen, Germany

[○]FS-SCS, Structural Dynamics with Ultra-short Pulsed X-rays, Deutsches Elektronen-Synchrotron (DESY), Notkestrasse 85, D-22607 Hamburg, Germany

S *Supporting Information*

ABSTRACT: Characteristics of nanoscale materials are often different from the corresponding bulk properties providing new, sometimes unexpected, opportunities for applications. Here we investigate the properties of 8 nm colloidal nanoparticles of MAPbBr$_3$ perovskites and contrast them to the ones of large microcrystallites representing a bulk. X-ray spectroscopies provide an exciton binding energy of 0.32 ± 0.10 eV in the nanoparticles. This is 5 times higher than the value of bulk crystals (0.084 ± 0.010 eV), and readily explains the high fluorescence quantum yield in nanoparticles. In the bulk, at high excitation concentrations, the fluorescence intensity has quadratic behavior following the Saha−Langmuir model due to the nongeminate recombination of charges forming the emissive exciton states. In the nanoparticles, a linear dependence is observed since the excitation concentration per particle is significantly less than one. Even the bulk shows linear emission intensity dependence at lower excitation concentrations. In this case, the average excitation spacing becomes larger than the carrier diffusion length suppressing the nongeminate recombination. From these considerations we obtain the charge carrier diffusion length in MAPbBr$_3$ of 100 nm.
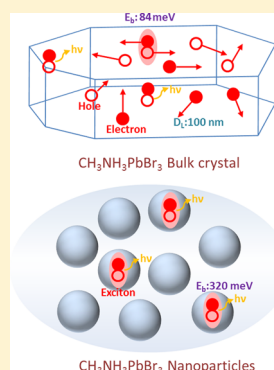
Organometal halide perovskites have attracted considerable attention as materials for low-cost optoelectronic devices. The advantages of such materials lay in facile solution-based chemical synthesis and a high absorption coefficient in a broad visible spectral range.[1−8] Furthermore, rapid dissociation of excitons to charges and slow recombination lead to long lifetime of the separated charges, which together with high charge mobility ensure simultaneously large diffusion length and efficient carrier transportation.[9−12] Besides photovoltaics applications, these materials have shown promise for light emitting diodes (LEDs) and lasing devices.[13−17] In films of the material, the exciton binding energy (E_b) is small, which explains the efficient exciton dissociation at room temperature.[18] Electrons and holes can meet again, forming excitons and emitting photons. The yield of emission critically depends on the electron−hole overlap, whereas the nonradiative trap/defect-mediated recombination reduces the emission effi-

ciency.[9,10,19,20] Solution-based synthesis typically leads to high concentration of such traps/defects.[21,22]

Semiconductor nanocrystals often show fascinating physical properties and opportunities for applications.[23] Recently, self-assembled methylammonium (MA) lead bromide perovskite (CH$_3$NH$_3$PbBr$_3$) nanocrystals in a solid organic matrix were demonstrated,[24] and Schmidt et al. reported synthesis of colloidal nanoparticles (NPs) of MAPbBr$_3$ with mean size of less than 10 nm.[25] The NPs show quantum confinement and high photoluminescence (PL) quantum yield (QY) ϕ_f = 17%—significantly more than in the corresponding bulk material (<0.1%).[26] What is the explanation of the high PL QY in MAPbBr$_3$ NPs? Usually, such enhancement is attributed to a high E_b and/or to passivation of nonradiative traps via capping

agent or core/shell structures.[27−29] Is it also the case here? The origin of the high ϕ_f and the nature of the emissive state in the perovskite NPs are the topics of the current Letter. We compare the electronic band alignment of colloidal MAPbBr$_3$ NPs with micrometer-size bulk-like crystallites (BCs) by using X-ray absorption and photoemission spectroscopy. We conclude that the E_b in the NPs is much larger than that in the bulk material. The high E_b leads to enhanced emission yield. We apply time-resolved PL spectroscopy to investigate the PL amplitude and kinetics as a function of excitation intensity. Differences in photoinduced excited state properties account for the enhanced PL in perovskite NPs and point out the potential of such materials in optoelectronic applications.

The NPs with mean size of 8.2 nm were synthesized following the technique reported in ref 25. For the BCs, the low concentration MAPbBr$_3$ precursor solution was spin coated on a glass substrate and annealed (for details of sample preparation and characterization, see Supporting Information, SI1,2). The absorption edge of the NPs shows an 8 nm blue-shift compared to the BCs (Figure 1). Considering that the Bohr radius of
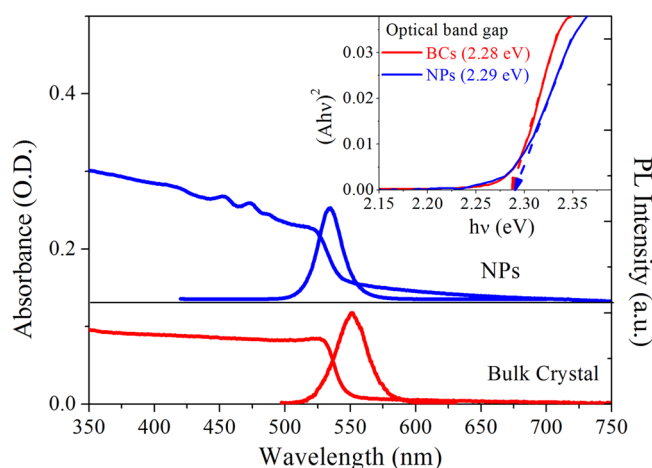

Figure 1. Steady-state UV−vis absorption spectra and photoluminescence spectra of the NPs and BCs. The zero baseline of the NP spectra is indicated by a horizontal line. The inset shows the Tauc plots ($(Ah\nu)^2 \sim h\nu$) calculated from the absorption spectra. A is the absorbance, and $h\nu$ is the photon energy. The optical band gaps were obtained by extrapolating the linear region of the Tauc plots to a zero level.

MAPbBr$_3$ is around 2 nm, the shift can be assigned to a weak quantum confinement effect in the NPs.[25] The emission spectrum of the NPs centered at 530 nm has a small Stokes shift of 8 nm. The emission of the BCs is centered at 551 nm, with a Stokes shift of 13 nm. The NPs also show additional absorption features at shorter wavelength (460−475 nm), which can be attributed to the formation of 2D MAPbBr$_3$ nanoplatelets. Their contribution is determined by the ratio of short-chain MA and long-chain octylammonium (OTA) precursors during the synthesis.[30−32] We can also observe some nanoplatelets in the transmission electron microscopy (TEM) images, but they are only minor species (for details, see SI3). Such 2D structures may affect the photoinduced dynamics of the NPs as will be discussed below. We can calculate the optical band gap of both samples from the Tauc plot ($(Ah\nu)^2 \sim h\nu$) of the absorption spectra.[33] The bandgap is 2.28 ± 0.01 eV and 2.29 ± 0.01 eV for the BCs and the NPs, respectively. (for details about the error evaluation, see SI4.)

In order to investigate the microscopic origin of the enhanced ϕ_f in the NPs, we first confirmed that $\phi_f = 17\%$ (see SI5), as reported earlier.[25] As we will show, the increase of the ϕ_f mainly originates from the high E_b preventing dissociation of the exciton prior to radiative decay. In order to establish the E_b value of the MAPbBr$_3$ NPs, we carry out a comparative study of the NPs and the BCs according to the following protocol, which has been previously elaborated for CdSe QDs.[34] We use X-ray photoemission spectroscopy (XPS) to establish the alignment of the valence band maxima (VBM) with respect to the Fermi level for the NPs and the BCs, as shown in Figure 2a. The alignment of the conduction band minimum (CBM), however, can only be determined utilizing a known reference. By making use of the E_b of the BCs (0.084 ± 0.010 eV) obtained by temperature-dependent photoluminescence measurements and the corresponding optical band gap extracted from Tauc plots (see Figure 1 inset), we can position the CBM of the BCs. The X-ray absorption measurements allow determining the mutual position of the two CBMs as shown in Figure 2b. Since we know the optical band gap of the NPs, we can now calculate their E_b. The details of the procedure are provided below.

Figure 2a displays the XPS spectra of the BCs and the NPs, showing the valence band (VB). The zero energy corresponds to the Fermi level. In order to better understand the electronic origin of the spectra we have calculated the local densities of states (lDOS) of the BCs by using the ab initio self-consistent real space multiple scattering approach implemented in the FEFF 9.0 code.[35,36] The results shown in Figure 2c are in good agreement with the experiment and with the literature data based on density functional theory (DFT) calculations.[37] The main valence feature displays two peaks centered at ∼4 and 5.5 eV, respectively. The photoionization cross sections of the possible orbitals contributing at the chosen photon energy (see SI6) show that the VB region has mainly Br 4p character. According to ref 36, the smaller peak at ∼5.5 eV consists of a σ bonding orbital formed by Pb 6s and halide 4p along Pb−Br−Pb, while the main peak at ∼4 eV corresponds to the analogous antibonding orbital.

The relative position of the VBM of the two samples with respect to their Fermi level are obtained from the crossing of the linear extrapolation of the band edge as shown in Figure 2a, with an uncertainty of ±0.05 eV. The VB spectrum of the NPs has a small but clearly distinguishable tail. Based on XPS measurements using 70 and 200 eV X-ray energy, we can assign this component to the surface of the NPs (for the details of surface component assignment, see SI7). We conclude that the VBM of the NPs is shifted by 0.2 eV below the VBM of the BCs. We also confirmed that the core emission from the Pb 4f and 4d levels of the NPs and the BCs are identical. This proves that the measured shift of the VBM of the NPs compared to that of the BCs is not due to any band-bending effect at the sample-substrate boundary (see SI8). The shift can be attributed to the combined effect of the distortion of the Pb−Br octahedral framework and the quantum confinement in the NPs.

The DOS calculation in Figure 2d shows that the dominant contribution to the CB edge is the Pb 6p orbital. This conclusion is consistent with other published work.[37] Clearly, it should be possible to determine the CBM from the photoinduced dipole-allowed Pb 4d to 6p transition. Here the Pb 4d$_{5/2}$ to 6p transition is too close to the N K edge to provide an accurate measurement. Therefore, the Pb N4
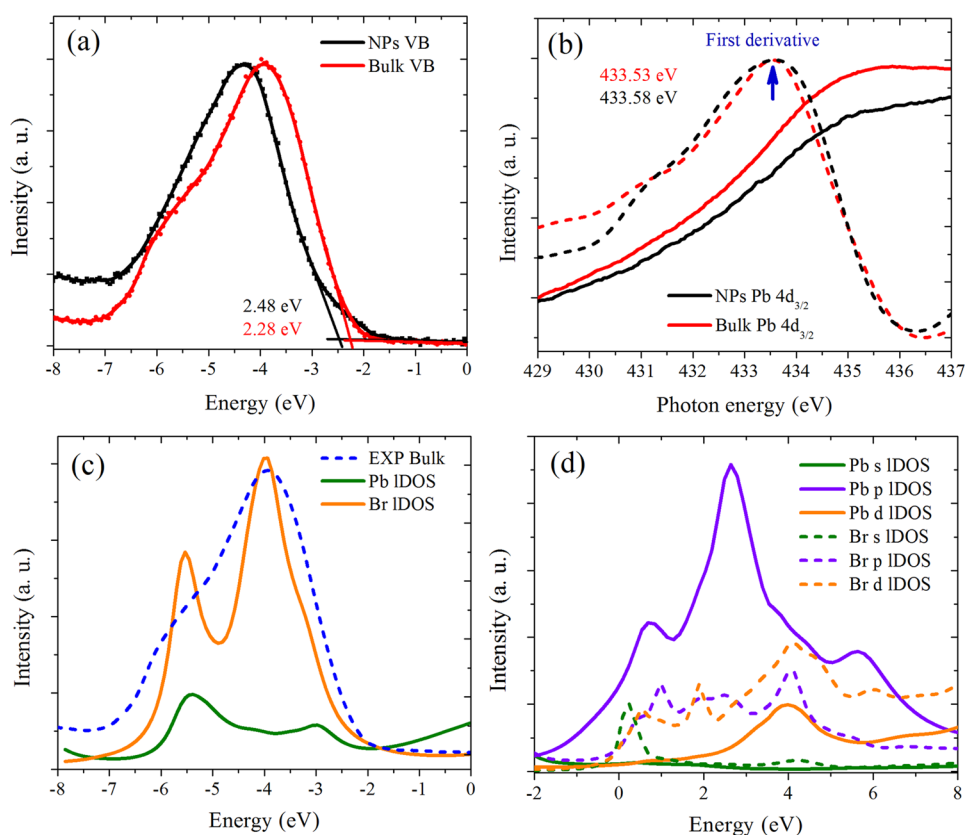
Figure 2. (a) XPS valence band spectra for the NPs and the BCs measured with an incident X-ray photon energy of 1000 eV. (b) Near edge X-ray absorption fine structure (NEXAFS) spectra at the Pb N4 edge corresponding to the photoionization of a $4d_{3/2}$ electrons measured in total electron yield mode. The absorption edges are determined from the position of the maximum in the first derivative of the rising edges (marked by the arrow). (c) Calculated lDOS compared to the experimental valence structure of the BCs. (d) Calculated lDOS in the CB. The dominant contribution to the CB edge is the Pb 6p orbital.

($4d_{3/2}$) absorption edge, corresponding to the photoionization of a $4d_{3/2}$ electron, was chosen. The rising edge of the X-ray absorption spectra shown in Figure 2b reflects mainly the Pb p DOS. The band edges of the two samples are determined from the maxima in the first derivative of the rising edges. This method eliminates possible errors generated from baseline subtraction and intensity normalization. We obtain very similar values where the CBM of NPs is 0.05 eV above the CBM of BCs. The difference is within the experimental uncertainty.[34]

In Figure 3 we have summarized the outcome of the measurements that yield an E_b of NPs 0.32 ± 0.10 eV for the NPs. This value is significantly larger than the E_b in the bulk and prevents exciton dissociation in the NPs. Since the mean size of the NPs is larger than the exciton Bohr radius (2 nm), the high E_b probably originates not only from confinement but also from other structural factors. This particular aspect is currently under investigation in our laboratory. Studying NPs of different sizes may be helpful to understand the relationship between the confinement and the E_b. However, at the current stage no protocol for systematic control of the NP size is available. A closely comparable E_b of 0.375 eV was very recently reported in slightly smaller MAPbBr$_3$ NPs based on the analysis of the temperature dependence of their integrated fluorescence intensity.[26]

For many applications, the band alignment with respect to the vacuum level is important. Therefore, the work functions of the two samples were measured by using XPS (see SI10). The

work function of the BCs and the NPs are 3.72 and 3.60 eV, respectively.

In order to investigate the consequences of the high E_b for the nature of the emitting state in the NPs, the time-resolved fluorescence in the NPs and the BCs was investigated. First we verified by streak camera measurements that the emission overwhelmingly originates from the band edge. In Figure 4 the fluorescence spectrograms of the two systems excited at 410 nm are presented. The negative time signal is due to the high repetition rate of the system (8 MHz) − a new excitation pulse arrives before the fluorescence from the previous excitation has fully decayed. The signal is clearly dominated by the band-edge fluorescence, while in the case of the NPs a negligible additional emission component can be seen at around 480 nm. This very weak emission is due to a minor contribution from the 2D nanoplatelets structures in the NP sample.[32] As mentioned above, they are also visible in the absorption spectrum. Since their emission is weak and decays rapidly, it does not influence the conclusions drawn from the following intensity dependent study.

Figure 5a,b shows a set of fluorescence kinetics at different laser fluences measured by time correlated single photon counting (TCSPC). In order to exclude the emission of 2D nanoplatelets impurities, a long-pass filter from 520 nm was used. Here the pulse repetition rate of the laser is significantly lower (2.5 MHz for the BCs and 100 kHz for the NPs), which means that the system has enough time to relax to the ground state before the new excitation pulse comes. No photo-
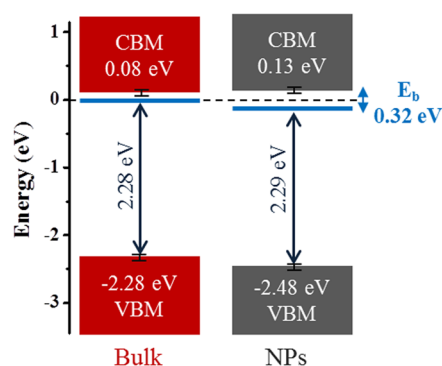
Figure 3. Band alignment between BCs and NPs. The zero energy level corresponds to the Fermi level. It should be noted that the electron−hole attraction responsible for the E_b affects both the energies of both electrons and holes. Therefore, the alignment of the optical band gap with the VBM is only for "visual convenience". The VBM was obtained from the XPS measurements. The electronic band gap is the sum of the optical band gap and the E_b. The absorption measurements provide the optical band gap 2.28 ± 0.01 eV for bulk and 2.29 ± 0.01 eV for NPs. The E_b of the BCs (0.084 ± 0.010 eV) obtained by the temperature dependent photoluminescence measurements (for details, see SI9) places the CBM of the BCs 0.04 eV above the Fermi energy. (A similar E_b value of bulk materials can also be found in the literature.[38]) The NEXAFS measurements enable concluding that the CBM of the BCs is 0.05 eV above the bulk CBM. The measured optical bandgap of 2.29 eV now allows determining the E_b of the NPs as 0.32 ± 0.1 eV, which is much larger than the bulk value.
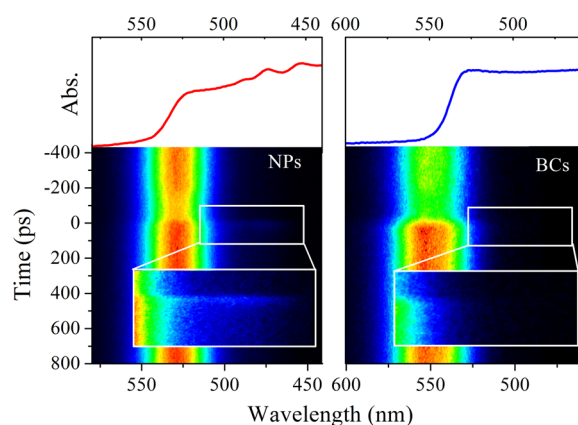

Figure 4. Time-resolved PL spectra of the NPs and the BCs obtained by streak camera ($\lambda_{exc} = 410$ nm, $I_{exc} = 2.1 \times 10^{12}$ ph/cm^2/pulse). The upper panels show the absorption spectra of the samples.

degradation of the samples during the measurement was observed (see SI11). The fluorescence kinetics exhibit complicated dependency upon the initial excitation concentration n_0 (where n_0 is defined as excitations/absorbed photons per volume element), and in this study, we only focus on PL_0 as a function of n_0 (for the absorption coefficient needed for n_0 calculation, see SI12). We point out that since the time resolution of the TCSPC is much longer than that of the streak camera system, any minor contribution from the fast dynamics related to the 2D nanoplatelets, which may have passed the filter, will then be even further reduced. In the log−log representation (see Figure 5c), the n_0 dependence of PL_0 has a very different behavior in the NPs and the BCs. The former has clearly a linear and the later mainly a quadratic dependence upon n_0. The balance ratio between the Wannier-Mott excitons

and charge carriers in bulk semiconductors resemble the ion−electron balance in a hot plasma and can be described by the Saha−Langmuir (SL) equation:[19]

$$\frac{x^2}{1-x} = \frac{1}{n}\left(\frac{2\pi\mu k_B T}{h^2}\right)^{1.5} e^{-E_b/k_B T}$$

(1)

where x is the fraction of free charges over the total density of excitation, n is the excitation density, and μ is the reduced mass of the exciton, which is 0.13 m_e for MAPbBr$_3$.[38]

The quadratic dependence of the initial emission intensity in the BCs agrees well with the SL model at higher n_0 and can be explained by nongeminate recombination of the free charges forming the emissive excitons. In the NPs and also at lower n_0 in the BCs, PL_0 has a linear n_0 dependence. In the NPs the linear behavior is expected since, even at the highest excitation intensities, the average number of excitations per NP is $\ll 1$. Analogously, in the case of the BCs, we also expect a deviation from the SL model once the excitation concentration is so small that the average distance between the excitations exceeds the diffusion length of the charges. The crossover between the two regimes occurs at the excitation concentration where the average distance is about 100 nm, providing an accurate estimate for the charge diffusion length in the MAPbBr$_3$ bulk material. Since all the BCs dimensions are in micrometer scale (see SI3) and more, the dimensionality does not influence the conclusion. The main uncertainly comes from the excitation concentration estimate, and we judge that the error in the diffusion length is about 30%. Our result is close to the reported diffusion lengths of solution processed methylamine trihaled materials, e.g., ~100 nm for MAPbI$_3$ film,[11,12] and 100 ± 50 nm for MAPbBr3(Cl) film.[39] These diffusion length values are much larger than those of the other solution-processed semiconductor materials such as conjugated polymers and colloidal quantum dot films, where they typically range from a few nanometers to tens of nanometers.[40−42] The diffusion length of perovskite materials is strongly dependent on density of defects.[43] In some special trap-free samples such as MAPbI$_x$Cl$_{1-x}$ mixed-halide films, large size single crystals, or chemical vapor processed MAPbI$_3$ films, the diffusion length can reach the micrometer scale.[12,44,45] The smaller diffusion length in our BCs samples indicates a relatively high defect density.

In summary, we have measured the exciton binding energy in MAPbBr$_3$ nanoparticles to be 0.32 eV, which is significantly higher than in the corresponding bulk material. This binding energy explains the high fluorescence quantum yield in the nanoparticles. The analysis of the initial photoinduced fluorescence amplitude reveals that, in the bulk material, the emission intensity follows a quadratic behavior at high n_0, clearly showing that the emission occurs from excitons after nongeminate recombination of charges. In the NPs the exciton dissociation probability is negligible due to the high binding energy, and consequently the emission probability is significantly increased. Even in the bulk, the initial emission intensity follows a linear dependence at lower n_0 since the recombination among the charges from different excitations becomes very unlikely once the distance between the excitations is larger than the diffusion length of the charges. This has allowed concluding accurately that the charge carrier diffusion length in the bulk of MAPbBr$_3$ is 100 nm.
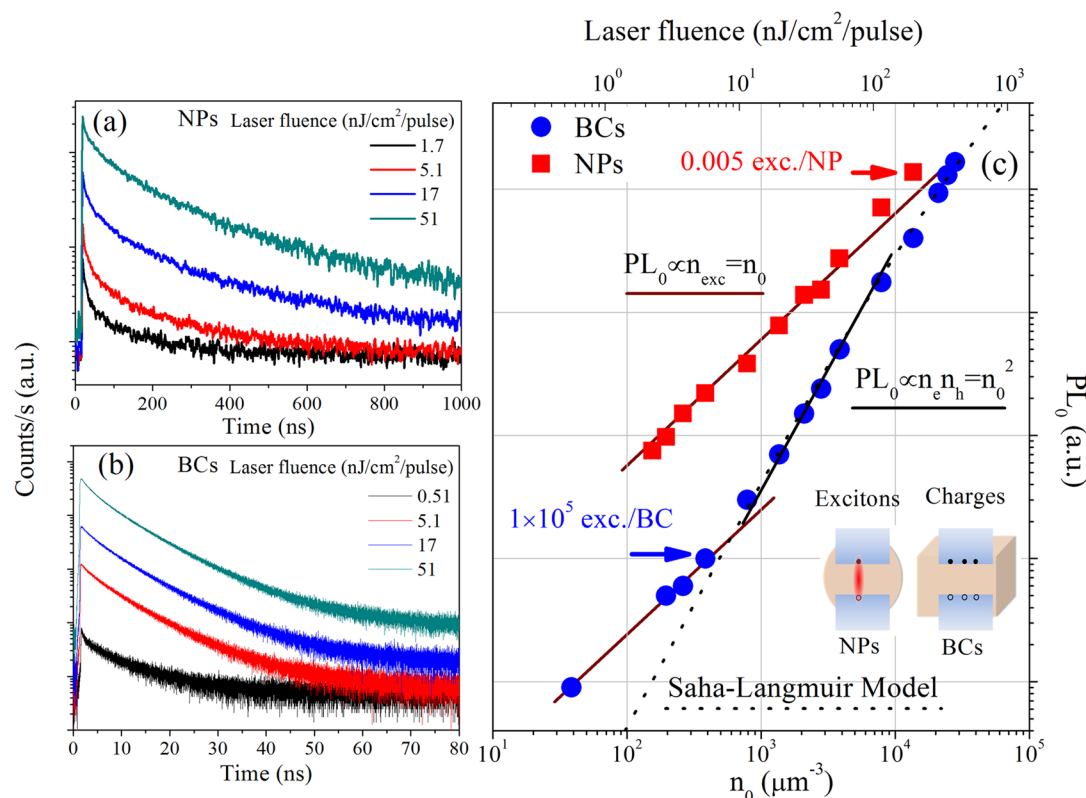
Figure 5. PL decay at different laser fluences (0.51−51 nJ/cm²/pulse, corresponding to excitation concentration of $1 \times 10^9 \sim 1 \times 10^{11}$ photons/cm²/pulse) for (a) the NPs and (b) the BCs. The intensity is normalized by the integration time of counting. (c) The initial PL intensity PL_0 as a function of excitation intensity. The inset illustrates the contribution of excitons vs charge carriers in two different samples.

■ ASSOCIATED CONTENT

ⓢ Supporting Information

Further details on experimental methods, size and morphology of the nanoparticles, calculation of photoluminescence quantum yield, absorption coefficient and excitation density, and detailed analysis on X-ray based characterization are available. The Supporting Information is available free of charge on the ACS Publications website at DOI: 10.1021/acs.jpclett.5b01252.

■ AUTHOR INFORMATION

Corresponding Authors
*E-mail: Tonu.Pullerits@chemphys.lu.se.
*E-mail: sophie.canton@desy.de.

Author Contributions

Kaibo Zheng, Qiushi Zhu, and Mohamed Abdellah contributed equally to this work.

Notes

The authors declare no competing financial interest.

■ ACKNOWLEDGMENTS

■ REFERENCES

(1) Lee, M. M.; Teuscher, J.; Miyasaka, T.; Murakami, T. N.; Snaith, H. J. Efficient hybrid solar cells based on meso-superstructured organometal halide perovskites. *Science* **2012**, *338*, 643−647.

(2) Kim, H. S.; Lee, C. R.; Im, J. H.; Lee, K. B.; Moehl, T.; Marchioro, A.; Moon, S.-J.; Humphry-Baker, R.; Yum, J. H.; Moser, J. E.; Grätzel, M.; Park, N. G. Lead Iodide Perovskite Sensitized All-Solid-State Submicron Thin Film Mesoscopic Solar Cell with Efficiency Exceeding 9%. *Sci. Rep.* **2012**, *2*, 591.

(3) Etgar, L.; Gao, P.; Xue, Z.; Peng, Q.; Chandiran, A. K.; Liu, B.; Nazeeruddin, M. K.; Grätzel, M. Mesoscopic $CH_3NH_3PbI_3/TiO_2$ Heterojunction Solar Cells. *J. Am. Chem. Soc.* **2012**, *134*, 17396−17399.

(4) Burschka, J.; Pellet, N.; Moon, S.-J.; Humphry-Baker, R.; Gao, P.; Nazeeruddin, M. K.; Grätzel, M. Sequential Deposition as a Route to High-Performance Perovskite-Sensitized Solar Cells. *Nature* **2013**, *499*, 316−319.

(5) Hodes, G. Perovskite-Based Solar Cells. *Science* **2013**, *342*, 317−318.

(6) Liu, M.; Johnston, M. B.; Snaith, H. J. Efficient Planar Heterojunction Perovskite Solar Cells by Vapour Deposition. *Nature* **2013**, *501*, 395−398.

(7) Mei, A.; Li, X.; Liu, L.; Ku, Z.; Liu, T.; Rong, Y.; Xu, M.; Hu, M.; Chen, J.; Yang, Y.; Gratzel, M.; Han, H. A Hole-Conductor-Free, Fully Printable Mesoscopic Perovskite Solar Cell with High Stability. *Science* **2014**, *345*, 295−298.

(8) Zhou, H.; Chen, Q.; Li, G.; Luo, S.; Song, T. B.; Duan, H. S.; Hong, Z.; You, J.; Liu, Y.; Yang, Y. Interface Engineering of Highly Efficient Perovskite Solar Cells. *Science* **2014**, *345*, 542−546.

(9) Ponseca, C. S.; Savenije, T. J.; Abdellah, M.; Zheng, K.; Yartsev, A.; Pascher, T.; Harlang, T.; Chabera, P.; Pullerits, T.; Stepanov, A.; Wolf, J.-P.; Sundström, V. Organometal Halide Perovskite Solar Cell Materials Rationalized: Ultrafast Charge Generation, High and Microsecond-Long Balanced Mobilities, and Slow Recombination. *J. Am. Chem. Soc.* **2014**, *136*, 5189−5192.

(10) Wehrenfennig, C.; Eperon, G. E.; Johnston, M. B.; Snaith, H. J.; Herz, L. M. High Charge Carrier Mobilities and Lifetimes in Organolead Trihalide Perovskites. *Adv. Mater.* **2014**, *26*, 1584−1589.

(11) Stranks, S. D.; Eperon, G. E.; Grancini, G.; Menelaou, C.; Alcocer, M. J. P.; Leijtens, T.; Herz, L. M.; Petrozza, A.; Snaith, H. J. Electron-Hole Diffusion Lengths Exceeding 1 Micrometer in an Organometal Trihalide Perovskite Absorber. *Science* **2013**, *342*, 341−344.

(12) Xing, G.; Mathews, N.; Sun, S.; Lim, S. S.; Lam, Y. M.; Grätzel, M.; Mhaisalkar, S.; Sum, T. C. Long-Range Balanced Electron- and Hole-Transport Lengths in Organic-Inorganic CH3NH3PbI3. *Science* **2013**, *342*, 344−347.

(13) Chondroudis, K.; Mitzi, D. B. Electroluminescence from an Organic−Inorganic Perovskite Incorporating a Quaterthiophene Dye within Lead Halide Perovskite Layers. *Chem. Mater.* **1999**, *11*, 3028−3030.

(14) Tan, Z. K.; Moghaddam, R. S.; Lai, M. L.; Docampo, P.; Higler, R.; Deschler, F.; Price, M.; Sadhanala, A.; Pazos, L. M.; Credgington, D.; Hanusch, F.; Bein, T.; Snaith, H. J.; Friend, R. H. Bright Light-Emitting Diodes Based on Organometal Halide Perovskite. *Nat. Nanotechnol.* **2014**, *9*, 687−692.

(15) Xing, G.; Mathews, N.; Lim, S.; Yantara, N.; et al. Low-Temperature Solution-Processed Wavelength-Tunable Perovskites for Lasing. *Nat. Mater.* **2014**, *13*, 476−480.

(16) Dohner, E.; Jaffe, A.; Bradshaw, L. R.; Karunadasa, H. I. Intrinsic White-Light Emission from Layered Hybrid Perovskites. *J. Am. Chem. Soc.* **2014**, *136*, 13154−13157.

(17) Deschler, F.; Price, M.; Pathak, S.; Klintberg, L. E.; Jarausch, D.; Higler, R.; Huttner, S.; Leijtens, T.; Stranks, S. D.; Snaith, H. J.; Atature, M.; Phillips, R. T.; Friend, R. H. High Photoluminescence Efficiency and Optically Pumped Lasing in Solution-Processed Mixed Halide Perovskite Semiconductors. *J. Phys. Chem. Lett.* **2014**, *5*, 1421−1426.

(18) Lin, Q.; Armin, A.; Nagiri, R. C. R.; Burn, P. L.; Meredith, P. Electro-optics of perovskite solar cells. *Nat. Photonics* **2015**, *9*, 106−112.

(19) D'Innocenzo, V.; Grancini, G.; Alcocer, M. J. P.; Kandada, A. R. S.; Stranks, S. D.; Lee, M. M.; Lanzani, G.; Snaith, H. J.; Petrozza, A. Excitons versus Free Charges in Organo-Lead Tri-Halide Perovskites. *Nat. Commun.* **2014**, *5*, 3586.

(20) Savenije, T. J.; Ponseca, C. S.; Kunneman, L.; Abdellah, M.; Zheng, K.; Tian, Y.; Zhu, Q.; Canton, S. E.; Scheblykin, I. G.; Pullerits, T.; Yartsev, A.; Sundström, V. Thermally Activated Exciton Dissociation and Recombination Control the Carrier Dynamics in Organometal Halide Perovskite. *J. Phys. Chem. Lett.* **2014**, *5*, 2189.

(21) Manser, J. S.; Kamat, P. V. Band Filling with Free Charge Carriers in Organometal Halide Perovskites. *Nat. Photonics* **2014**, *8*, 737−743.

(22) Stranks, S. D.; Burlakov, V. M.; Leijtens, T.; Ball, J. M.; Goriely, A.; Snaith, H. J. Recombination Kinetics in Organic-Inorganic Perovskites: Excitons, Free Charge, and Subgap States. *Phys. Rev. Appl.* **2014**, *2*, 034007.

(23) Zheng, K.; Karki, K.; Zidek, K.; Pullerits, T. Ultrafast photoinduced dynamics in quantum dot-based systems for light harvesting. *Nano Res.* **2015**, *8*, 2125−2142.

(24) Di, D.; Musselman, K. P.; Li, G.; Sadhanala, A.; Ievskaya, Y.; Song, Q.; Tan, Z.; Lai, M. L.; MacManus-Driscoll, J. L.; Greenham, N. C.; Friend, R. H. Size-Dependent Photon Emission from Organometal Halide Perovskite Nanocrystals Embedded in an Organic Matrix. *J. Phys. Chem. Lett.* **2015**, *6*, 446−450.

(25) Schmidt, L. C.; Pertegas, A.; Gonzalez-Carrero, S.; Malinkiewicz, O.; Agouram, S.; Minguez Espallargas, G.; Bolink, H.; Galian, R. E.;

(26) Zhang, F.; Zhong, H.; Chen, C.; Wu, X. G.; Hu, X.; Huang, H.; Han, J.; Zou, B.; Dong, Y. Brightly Luminescent and Color-Tunable Colloidal CH3NH3PbX3 (X = Br, I, Cl) Quantum Dots: Potential Alternatives for Display Technology. *ACS Nano* **2015**, *9*, 4533−4542.

(27) Reiss, P.; Protière, M.; Li, L. Core/Shell Semiconductor Nanocrystals. *Small* **2009**, *5*, 154−168.

(28) Biadala, L.; Siebers, B.; Gomes, R.; et al. Tuning Energy Splitting and Recombination Dynamics of Dark and Bright Excitons in CdSe/CdS Dot-in-Rod Colloidal Nanostructures. *J. Phys. Chem. C* **2014**, *118*, 22309−22316.

(29) Zídek, K.; Zheng, K.; Abdellah, M.; Lenngren, N.; Chábera, P.; Pullerits, T. Ultrafast Dynamics of Multiple Exciton Harvesting in the CdSe-ZnO System: Electron Injection versus Auger Recombination. *Nano Lett.* **2012**, *12*, 6393−6399.

(30) Takeoka, Y.; Fukasawa, M.; Matsui, T.; Kikuchi, K.; Rikukawa, M.; Sanui, K. Intercalated formation of two-dimensional and multi-layered perovskites in organic thin films. *Chem. Commun.* **2005**, *3*, 378−380.

(31) Audebert, P.; Clavier, G.; Alain-Rizzo, V. R.; Deleporte, E.; Zhang, S.; Lauret, J.-S. B.; Lanty, G. T.; Boissière, C. D. Synthesis of New Perovskite Luminescent Nanoparticles in the Visible Range. *Chem. Mater.* **2009**, *21*, 210−214.

(32) Tyagi, P.; Arveson, M. S.; Tisdale, W. A. Colloidal Organohalide Perovskite Nanoplatelets Exhibiting Quantum Confinement. *J. Phys. Chem. Lett.* **2015**, *6*, 1911−1916.

(33) Tauc, J. Optical Properties and Electronic Structure of Amorphous Ge and Si. *Mater. Res. Bull.* **1968**, *3*, 37−46.

(34) Meulenberg, R. W.; Lee, J. R. I.; Wolcott, A.; Zhang, J. Z.; Terminello, L. J.; Van Buuren, T. Determination of the Exciton Binding Energy in CdSe Quantum Dots. *ACS Nano* **2009**, *3*, 325−330.

(35) Rehr, J. J.; Kas, J. J.; Vila, F. D.; Prange, M. P.; Jorissen, K. Parameter-free calculations of X-ray spectra with FEFF9. *Phys. Chem. Chem. Phys.* **2010**, *12*, 5503−5513.

(36) Swarbrick, J. C.; Skyllberg, U.; Karlsson, T.; Glatzel, P. High Energy Resolution X-ray Absorption Spectroscopy of Environmentally Relevant Lead(II) Compounds. *Inorg. Chem.* **2009**, *48*, 10748−10756.

(37) Lindblad, R.; Bi, D.; Park, B.; Oscarsson, Johan.; Gorgoi, M.; Siegbahn, H.; Odelius, M.; Johansson, E. M. J.; Rensmo, H. Electronic structures of TiO2/CH3NH3PbI3 perovskite solar cell interfaces. *J. Phys. Chem. Lett.* **2014**, *5*, 648−653.

(38) Tanaka, K.; Takahashi, T.; Ban, T.; Kondo, T.; Uchida, K.; Miura, N. Comparative Study on the Excitons in Lead-Halide-Based Perovskite-Type Crystals CH3NH3PbBr3 CH3NH3PbI3. *Solid State Commun.* **2003**, *127*, 619−623.

(39) Kedem, N.; Brenner, T. M.; Kulbak, M.; Schaefer, N.; Levcenko, S.; Levine, I.; Abou-Ras, D.; Hodes, G.; Cahen, David. Light-Induced Increase of Electron Diffusion Length in a p−n Junction Type CH3NH3PbBr3 Perovskite Solar Cell. *J. Phys. Chem. Lett.* **2015**, *6*, 2469−2476.

(40) Shaw, P. E.; Ruseckas, A.; Samuel, I. D. W. Exciton Diffusion Measurements in Poly(3-hexylthiophene). *Adv. Mater.* **2008**, *20*, 3516−3520.

(41) Tada, A.; Geng, Y.; Wei, Q.; Hashimoto, K.; Tajima, K. Tailoring Organic Heterojuction Interfaces in Bilayer Polymer Photovoltaic Devices. *Nat. Mater.* **2011**, *10*, 450−455.

(42) Zheng, K.; Žídek, K.; Abdellah, M.; Zhu, N.; Chabera, P.; Lenngren, N.; Chi, Q.; Pullerits, T. Directed Energy Transfer in Films of CdSe Quantum Dots: Beyond the Point Dipole Approximation. *J. Am. Chem. Soc.* **2014**, *136*, 6259−6268.

(43) Buin, A.; Pietsch, P.; Xu, J.; Voznyy, O.; Ip, A. H.; Comin, R.; Sargent, E. H. Materials Processing Routes to Trap-Free Halide Perovskites. *Nano Lett.* **2014**, *14*, 6281−6286.

(44) Sheng, R.; Ho-Baillie, A.; Huang, S.; Chen, S.; Wen, X.; Hao, X.; Green, M. A. Methylammonium Lead Bromide Perovskite-Based Solar Cells by Vapor-Assisted Deposition. *J. Phys. Chem. C* **2015**, *119*, 3545−3549.

Perez-Prieto, J. Nontemplate Synthesis of CH3NH3PbBr3 Perovskite Nanoparticles. *J. Am. Chem. Soc.* **2014**, *136*, 850−853.

(45) Dong, Q.; Fang, Y.; Shao, Y.; Mulligan, P.; Qiu, J.; Cao, L.; Huang, J. Electron-hole diffusion lengths >175 μm in solution-grown CH$_3$NH$_3$PbI$_3$ single crystals. *Science* **2015**, *347*, 967−970.